frontiers in Energy Research

ORIGINAL RESEARCH
published: 09 March 2021
doi: 10.3389/fenrg.2020.605976

In Situ Spectroelectrochemical Investigation of Perovskite Quantum Dots for Tracking Their Transformation

ChaeHyun Lee[1†‡], Kyoungsoo Kim[2†‡], YeJi Shin[1‡], Donghoon Han[2‡] and Seog Joon Yoon[1*‡]*

[1]Department of Chemistry, College of Natural Science, Yeungnam University, Gyeongsan, South Korea, [2]Department of Chemistry, The Catholic University of Korea, Bucheon, South Korea

OPEN ACCESS

Edited by:
Jin Won Kim,
Drexel University, United States

Reviewed by:
Huan Pang,
Yangzhou University, China
Kaibo Zheng,
Technical University of Denmark, Denmark

***Correspondence:**
Donghoon Han
dhan@catholic.ac.kr
Seog Joon Yoon
yoon@yu.ac.kr

[†]These authors have contributed equally to this work.

[‡]ORCID:
ChaeHyun Lee
orcid.org/0000-0002-5300-6049
Kyoungsoo Kim
orcid.org/0000-0001-5853-7247
YeJi Shin
orcid.org/0000-0002-7098-7299
Donghoon Han
orcid.org/0000-0003-1870-3006
Seog Joon Yoon
orcid.org/0000-0002-8921-9062

Specialty section:
This article was submitted to Electrochemical Energy Conversion and Storage, a section of the journal Frontiers in Energy Research

Received: *14 September 2020*
Accepted: *26 November 2020*
Published: *09 March 2021*

Citation:
Lee C, Kim K, Shin Y, Han D and Yoon SJ (2021) In Situ Spectroelectrochemical Investigation of Perovskite Quantum Dots for Tracking Their Transformation. Front. Energy Res. 8:605976. doi: 10.3389/fenrg.2020.605976

All-inorganic lead-halide perovskite quantum dots (PQDs) ($CsPbX_3$, where X is Cl, Br, or I) have been used successfully in optoelectronic applications, such as solar cells, light-emitting diodes, photocatalysts, and lasers. These PQDs work under electrochemical bias and/or illumination with charge separation/collection by interacting with the charge-transport medium. In this study, we discuss the spectroelectrochemical characteristics of PQDs to understand the oxidation and reduction processes that occur during photoinduced charge transport or charge injection under electrochemical conditions. We also found that the PQDs underwent irreversible transformation to the precursor state of plumbate complexes under electrochemical conditions. Furthermore, *in situ* spectroelectrochemical analysis demonstrated that hole-mediated electrochemical oxidation of PQDs resulted in their irreversible transformation. Finally, the results presented herein contribute to our understanding of the charge-transfer-mediated process in PQDs and enhance their application potential in optoelectronic devices.

Keywords: all-inorganic lead-halide perovskite, perovskite quantum dot, spectroelectrochemistry, *in situ* detection, irreversible transformation

INTRODUCTION

Ever since Mitzi et al. described perovskites and their unique properties for optoelectronic applications in the 1990s, hybrid organic–inorganic perovskites have attracted significant attention owing to their versatile and outstanding photophysical properties (Mitzi et al., 1995; Kagan et al., 1999; Mitzi et al., 1999). Various ABX_3-type hybrid perovskites ($A = MA^+$, FA^+, and Cs^+, where $MA^+ = CH_3NH_3^+$ and $FA^+ = CH(NH_2)^{2+}$, $B = Pb^{2+}$ and Sn^{2+}, and $X = Cl^-$, Br^-, and I^-) have been studied for their intrinsic structural (Gebhardt and Rappe, 2019) and photophysical properties (Chen et al., 2018). They have been found to exhibit a large grain layering up to the micron level (Chen et al., 2015b), fast charge transport (Senanayak et al., 2017), long diffusion lengths in the range of several micrometers (Dong et al., 2015), absorption cross-sections larger than 10^5 cm^{-1} (Wang et al., 2019), and low exciton binding energies (16–32 meV), which are comparable to the thermal energy (k_BT) at room temperature and thus can facilitate free carrier generation (Saba et al., 2014). One outstanding achievement in this area is increasing the photoconversion efficiency (PCE) of perovskite-based solar cells from 3.8% (Kojima et al., 2009) to 25.2% in 2020 (NREL, 2020). These efforts represent an important turning point; for the first time, a PCE greater than 20% has been achieved, which suggests the practical use of perovskites in the commercial market. In addition, high stability (Zhao and Zhu, 2016), large-module fabrication (Zhao and Zhu, 2016; Agresti et al., 2019), and methodological developments, such as screen printing (Rong et al., 2018) and spray pyrolysis (Bishop et al., 2018), enhance the application potential of perovskites. For example, perovskites have been used in various optoelectronic devices, such as lasers (Jia et al., 2016), photocatalysis (Zhang et al., 2015; Li et al., 2017; Huang et al., 2020), hydrogen-evolution reactors (Kim et al., 2019; Zheng et al., 2019), and light-emitting diodes (Sadhanala et al., 2015).

In optoelectronic devices, perovskites exhibit a unique photoelectrochemical behavior depending on the applied bias or illumination. They exhibit several intriguing phenomena, such as current density–voltage (*J–V*) hysteresis (Chen et al., 2015a), phase segregation in mixed halide perovskites (Hoke et al., 2015; Yoon et al., 2016a), charge/ion accumulation at interfaces (Zolfaghari et al., 2018), charge-recombination mechanisms that are dependent on illumination conditions (Draguta et al., 2016), and selective electron/hole-mediated redox processes (Samu et al., 2019). The origin of *J–V* hysteresis is still a controversial issue, but one possible explanation is ion migration combined with nonradiative recombination at the grain boundary through charge accumulation (Weber et al., 2018; Kang and Park, 2019). Perovskites have several defects, such as Schottky defects, Frenkel defects, lattice distortion by accumulated charges or impurities, lamination, piezoelectric effect, and surface defects (Yuan and Huang, 2016). Therefore, ion migration might be induced in several ways; however, one kinetically favorable ion-migration mechanism is migration through ion vacancies, especially in ABI_3 or $ABBr_xI_{3-x}$ iodide-based perovskites (Yuan and Huang, 2016; Kang and Park, 2019; Brennan et al., 2020). This phenomenon indicates that hybrid perovskites are softened materials that can induce ion migration, structural changes under an applied bias, charge trapping at defect sites, and piezoelectric effect (Yuan and Huang, 2016). Kamat and coworkers studied the spectroelectrochemistry of 3D bulk perovskite films and provided insights into the photoinduced oxidation/reduction processes in bulk $MAPbX_3$/$CsPbX_3$ films and the impact of the electrochemical environment on photochemistry (Samu et al., 2018; Samu et al., 2019). In addition, selective hole-mediated oxidation occurred in mixed halide perovskites when the applied bias matched with the energy level of halide vacancies (Samu et al., 2019). Hole-mediated oxidation resulted in the oxidation of iodide components, rather than bromide components, in mixed halide perovskites due to lower migration energy of the former and higher Pb complexation constants of the latter (Yoon et al., 2016b). Therefore, it is crucial to consider the effect of electrical field during optoelectronic device operation.

When the crystallite size of perovskites decreases to the exciton Bohr diameter (5, 7, and 12 nm for $CsPbCl_3$, $CsPbBr_3$, and $CsPbI_3$, respectively), the materials exhibit bandgap tunability via the quantum confinement effect (Protesescu et al., 2015). It has been reported that PQDs show outstanding lucidity, with a photoluminescence quantum yield (PLQY) more than 80%. Kovalenko and coworkers developed strategies for PQD synthesis, with cubic cores covered by long carbon chain ligands, such as oleic acid (OA) or oleylamine (OAm). Thus far, the highest photovoltaic performance reported for PQD-based solar cells was 15.6% (Li et al., 2019); interestingly, in the PQD-based solar cells, *J–V* hysteresis, charge accumulation, and ion migration at interfaces between PQDs and TiO_2 layers (Zolfaghari et al., 2018).

Several studies on all-inorganic PQDs employed photoelectrochemical tools to understand band-edge position (Noh et al., 2013; Cardenas-Morcoso et al., 2019), redox events (Samu et al., 2018), photocatalytic activity for the degradation of organic molecules (Gualdron-Reyes et al., 2019), hydrogen evolution (Chen et al., 2015c), and water splitting (Chen et al., 2018). However, it is important to evaluate the role of PQDs as catalysts as well instead of considering them as primary reactants alone. In addition, to understand the effect of electrical field on the optical properties of PQDs, it is important to consider the effect of possible redox processes at defect-mediated energy levels and/or band edges.

Therefore, in this study, we investigated the impact of the spectroelectrochemical environment on the photophysical properties of PQDs dispersed in colloidal solutions. The defect-mediated oxidation of PQDs was characterized by cyclic voltammetry (CV), which is an irreversible process, by inducing hole-mediated transformation using an applied positive bias. Through *in situ* detection by UV-Vis absorption spectroscopy, we observed that the PQDs returned to the precursor state as plumbate complexes at a critical potential. The results obtained herein illustrate how imperfect structural constructs in PQDs participate in the electrochemical oxidation and irreversible transformation processes. Furthermore, the spectroelectrochemical analysis approach presented herein lays the foundation for engineering optoelectronic devices, such as PQD-based solar cells, photocatalysts, and water-splitting groups.

MATERIALS AND METHODS

Chemicals

Cesium carbonate (Cs_2CO_3, Samchun Chemicals, 99.5%), OA (Alfa Aesar, 90%), 1-octadecene (1-ODE) (Sigma-Aldrich, 90%), PbI_2 (TCI, 99.999%), (Aldrich, 99%), $PbBr_2$ (Alfa Aesar, 98%), oleylamine (OAm, TCI, 50%), n-hexane (Daejung, 95%), and riboflavin (Daejung, 98%) were used to synthesize PQDs and study their basic photophysical properties. Initially, 1-ODE was heated to 120°C and cooled down to reduce residual H_2O in the solvent; this purified solvent was used for subsequent synthesis reactions. All other chemicals were used as received without further purification. For spectroelectrochemical measurements, dichloromethane (DCM, ≥99.5%, Sigma-Aldrich) and tetrabutylammonium hexafluorophosphate (TBAFP, 98%, Sigma-Aldrich) were used. All chemicals for electrochemical/spectroelectrochemical characterization were used as received.

Synthesis of $CsPbX_3$ (X: Br or I) Perovskite Quantum Dots

We slightly modified the procedure reported in literature for synthesizing $CsPbX_3$ (X: Br or I) PQDs (Protesescu et al., 2015;

Gualdrón-Reyes et al., 2018). Briefly, a cesium oleate precursor solution was prepared by loading Cs_2CO_3 (0.407 g), OA (1.25 ml), and 1-ODE (20 ml) in a 50 ml three-neck flask under vacuum for 30 min at 80°C. After 30 min, the mixture was heated under vacuum to 120°C for another 30 min; finally, it was heated to 140°C in N_2 atmosphere until Cs_2CO_3 dissolved completely in OA. The solution was continuously preheated at 115°C with N_2 purging to inhibit Cs-oleate precipitation. When the Cs-oleate solution turns dark orange, it indicates Cs-oleate oxidation to form Cs_2O. PbI_2 (0.5 g) ($PbBr_2$, 0.4 g) and 1-ODE (50 ml) were reacted in another 100 ml three-neck flask to synthesize $CsPbI_3$ ($CsPbBr_3$) QDs. The mixture was dried under vacuum for 30 min at 120°C. Subsequently, 2.5 ml of each of OA and OAm was loaded in a 50 ml beaker at 130°C. The solution was swiftly injected into the flask when it turned yellow. When the mixture was completely dissolved, the temperature of the reaction was increased to 170°C and 2 ml of the Cs-oleate solution was quickly injected into the flask. After reaction, the flask was cooled in an ice bath until it reached a temperature of 60–70°C. To obtain fresh colloidal PQD solutions, the as-synthesized solutions were centrifuged for 10 min at 6,000 rpm and the supernatant was discarded. The precipitants were then dispersed in 10 ml of hexane until further use.

Material Characterization

X-ray diffraction (XRD), field emission scanning microscopy (FE-SEM), and field emission transmission electron microscopy (FE-TEM) were conducted to analyze the crystalline structure and morphology of the synthesized PQDs. XRD patterns were collected on a D8 Advance (Bruker) using Cu–Kα radiation in the 2θ range of 10°–80° (0.05°/step and 0.5 s/step). Cu–$K\alpha_2$ peak stripping was performed using the Eva® program. SU8010 (Hitach) FE-SEM was used to observe topographic images of PQDs. A Tecnai G2 F20 S-TWIN (FEI Korea) instrument was used for FE-TEM and selective area electron diffraction (SAED) analysis.

Steady-State Absorption and Emission

To analyze the steady-state absorption and emission characteristics of colloidal $CsPbX_3$ QD solutions, UV-Vis absorption and photoluminescence (PL) spectrophotometry were conducted on a Duetta (HORIBA Scientific) instrument. The PLQY of QDs was measured as a relative value compared to the PLQY of riboflavin, which was set at 0.3 (Koziol, 1966). An excitation wavelength of 430 nm was used to measure the PL of QDs and riboflavin. To prevent self-absorption, absorption at the excitation wavelength (430 nm) was fixed at 0.1.

Electrochemical Characterization

All electrochemical experiments were conducted using a CH Instruments electrochemical analyzer (Model 760E) in a standard three-electrode cell using glassy carbon (GC) (4 mm in diameter) and gold (1.6 mm in diameter) electrodes as the working electrodes and a Pt wire as the counter electrode. An Ag/Ag^+ electrode consisting of 0.01 M $AgNO_3$ and 0.1 M tetrabutylammonium hexafluorophosphate (TBAFP) in acetonitrile as an organic solution and an Ag/AgCl electrode as an aqueous solution were used as reference electrodes. Before conducting the experiments, the working electrodes were polished with 0.3 μm alumina (Buehler, United States) on a polishing cloth and thoroughly rinsed with deionized water, acetonitrile, and acetone. Prior to measurement, all the supporting electrolyte solutions were purged with N_2 gas for at least 20 min. All electrochemical experiments were conducted at room temperature (20–25°C).

Fabrication of $CsPbBr_3$ Films

Indium tin oxide (ITO) coated glass slides (60 × 9 mm^2, 1.1 mm thick, Wooyang GMS, Korea) were used as substrates. Initially, these slides were sequentially cleaned with ethanol, acetone, and deionized water. After removing moisture from slide surfaces with an air blower, they were dehydrated on a hot plate at 120°C for 3 min and then cooled to room temperature. Subsequently, the colloidal $CsPbBr_3$ solution was spin-coated (SC-100RPM-C, RHABDOS, Korea) on substrate surfaces at 3,000 rpm for 30 s. Finally, $CsPbBr_3$-coated ITO substrates were heated on a hot plate at 220°C for 3 min and then allowed to cool down to room temperature.

Spectroelectrochemistry

UV-Vis absorption spectra were obtained on a UV-Vis absorption spectrophotometer (AvaSpec-ULS2048, AVANTES, Netherlands). This integrated system allows control over the potentiostat (WaveDriver 200, Pine Research Instrumentation, United States) and spectrophotometer and synchronizes electrochemical measurements with spectroscopic measurements. A spectroelectrochemical cell comprising of a gold-patterned honeycomb electrode (Pine Research Instrumentation, United States) was used as the working electrode, while Au electrode was used as the counter electrode and Ag/Ag^+ was used as the reference electrode. The gold-patterned honeycomb electrode was rinsed in deionized water before being cleaned with acetone using a sonicator. Furthermore, it was cleaned by electrochemical oxidation and reduction in 0.5 M H_2SO_4 by applying a positive potential of +2.0 V for 5 s, followed by a negative potential of −0.35 V. Repetitive CV experiments were conducted in the potential range of −0.3 to +1.55 V at a scan rate of 4 V/s in 0.5 M H_2SO_4 until a reproducible result was achieved (Han et al., 2009). To simultaneously investigate the electrochemical process and changes in the UV-Vis absorption spectra, the potential was increased at 10 s intervals toward oxidizing and reducing potentials at the same time as monitoring the changes in absorbance with respect to the applied potential.

RESULTS AND DISCUSSION

Structural Properties of Perovskite Quantum Dots

In this study, we used colloidal $CsPbBr_3$ and $CsPbI_3$ PQD-dispersed solutions to determine the impact of electrochemical environment on their photophysical properties. All-inorganic $CsPbBr_3$ and $CsPbI_3$ PQDs were synthesized by the hot-injection

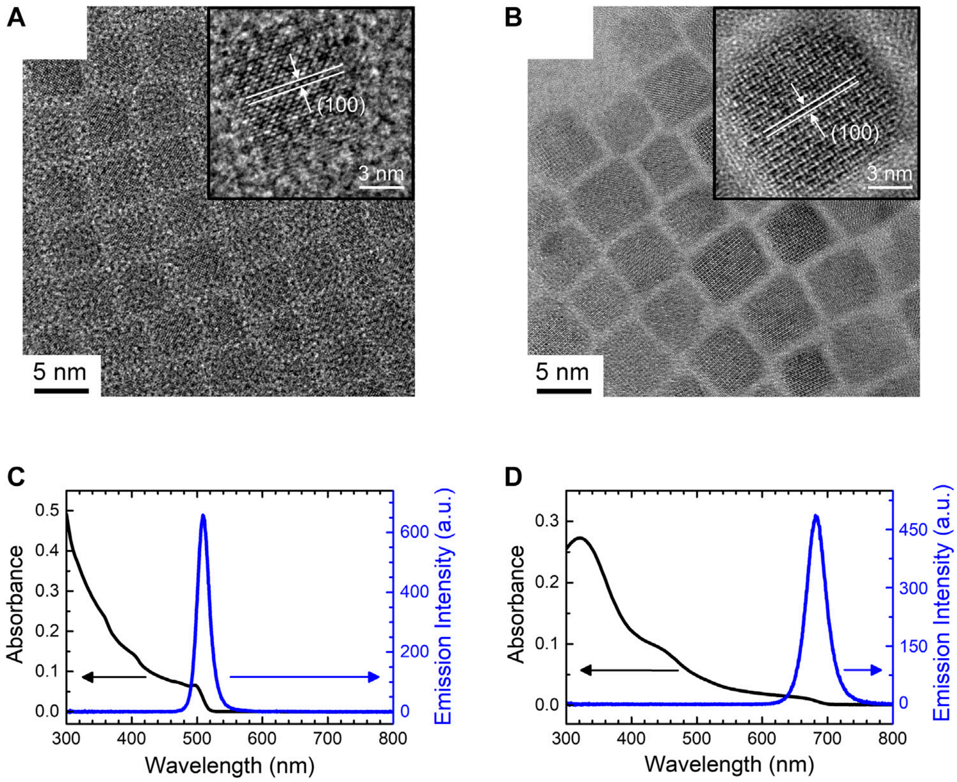

FIGURE 1 | TEM images of **(A)** $CsPbBr_3$ and **(B)** $CsPbI_3$ PQDs. The insets show enlarged views of individual PQDs. UV-Vis absorption and PL spectra of **(C)** $CsPbBr_3$ and **(D)** $CsPbI_3$ colloidal PQD solutions.

process, as described in the literature (Protesescu et al., 2015; Gualdrón-Reyes et al., 2018). We firstly used FE-SEM to observe general unity of PQDs' shape and aspect ratio. For both $CsPbBr_3$ (**Supplementary Figure S1A**) and $CsPbI_3$ (**Supplementary Figure S1B**) PQDs, similar sizes (~10 nm) and round shaped PQDs were able to be observed. However, due to massively stacked PQD layers on substrate, details of each PQD were not able to characterize. **Figures 1A,B** show the TEM images of $CsPbBr_3$ and $CsPbI_3$ PQD monolayers, respectively, with the corresponding lattice fringes in the insets. The observed lattice fringes matched the (100) planes detected by XRD in both $CsPbBr_3$ and $CsPbI_3$ PQDs (**Supplementary Figure S2**). SAED patterns (**Supplementary Figure S3**) were also recorded and it was found that there was an excellent agreement between these patterns and XRD results in **Supplementary Figure S2**. The SAED patterns further suggested that the $CsPbBr_3$ and $CsPbI_3$ PQDs exhibited cubic and orthorhombic crystalline structures, respectively. Each spotted circular pattern was integrated for each crystalline PQD in **Figures 1A,B**. The clear fit between the lattice fringes observed by TEM and those derived from XRD and SAED confirms the nanocrystalline shape and structure of the studied PQDs. Both $CsPbBr_3$ and $CsPbI_3$ PQDs exhibited a cubic particle shape with sizes of (9.3 ± 1.6) and (11.3 ± 2.0) nm, respectively (**Figure S4**). The polydispersity values (ratio of the standard deviation in PQD size and the actual size of PQDs) of $CsPbBr_3$ and $CsPbI_3$ PQDs were found to be 17.2% and 17.7%, respectively. The sudden burst of nucleation in the hot-injection process enables the simultaneous growth of PQDs with sizes similar to the exciton Bohr diameter. The narrow size distribution of $CsPbBr_3$ and $CsPbI_3$ PQDs resulted in their narrow PLs with full-width at half maximum of 20 nm for $CsPbBr_3$ PQDs and 35 nm for $CsPbI_3$ PQDs (see **Figures 1C,D**). The distinct emission peak maxima observed at 508 and 683 nm for $CsPbBr_3$ and $CsPbI_3$ PQDs, respectively, indicate clear band gaps of 2.44 and 1.82 eV. The PLQY of the two PQD systems was measured by comparing with that of a standard dye, riboflavin, using the following equation:

$$\phi_{\text{PQDs}} = \phi_{\text{standard}}\left(\frac{Emission\ Area_{PQDs}}{Emission\ Area_{\text{standard}}}\right)\left(\frac{\eta^2_{\text{PQDs}}}{\eta^2_{\text{standard}}}\right), \quad (1)$$

where ϕ_{PQDs}, $\phi_{standard}$, $\eta_{PQDs,}$ and $\eta_{standard}$ represent the mean PLQY of the tested PQDs, PLQY of the dye, refractive index of the PQD solution (n-hexane), and refractive index of the dye solution (ethanol), respectively. Using this equation, the PLQYs of $CsPbBr_3$ and $CsPbI_3$ PQDs were calculated to be 37.6% and 45.8%, respectively. In these two highly emissive $CsPbBr_3$ and $CsPbI_3$ PQDs, photoexcited electron-hole recombination occurred mainly due to radiative recombination between the conduction band minimum (CBM) and valence band maximum (VBM). Thus far, we have fabricated crystalline emissive PQDs with small size distributions and continuously observed their photoelectrochemical behavior. However,

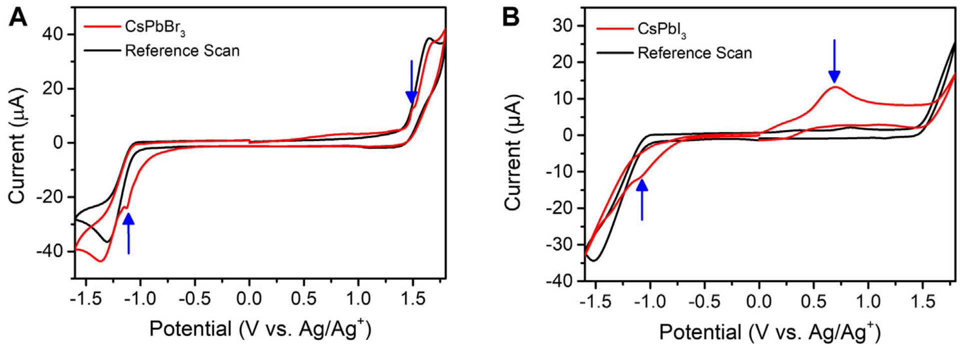

FIGURE 2 | (A) CV of $CsPbBr_3$ dispersed in DCM containing 0.1 M TBAFP (scan rate of 50 mV/s) in the absence (black line) and presence (red line) of PQDs at the GC electrode. **(B)** CV of $CsPbI_3$ dispersed in DCM containing 0.02 M TBAFP (scan rate of 50 mV/s) in the absence (black line) and presence (red line) of PQDs at the GC electrode.

nonradiative recombination from various trap sites, such as internal and surface defect-mediated traps, in these PQDs cannot be ignored.

Electrochemical Behavior of the Perovskite Quantum Dots and Irreversible Transformation

To evaluate the redox processes at energy levels in the PQDs, we investigated the electrochemical response of the colloidal PQD solutions. **Figures 2A,B** show the CV curves of $CsPbBr_3$ and $CsPbI_3$ in DCM containing the TBAFP-supporting electrolyte obtained from the GC electrode. The CV curves obtained in the presence of the PQDs showed distinct redox peaks when compared to those obtained in the absence of the PQDs. The resulting VBM and CBM energy levels were derived from the equations $E_{CBM} = -(4.5 + E_{red})$ and $E_{VBM} = -(4.5 + E_{oxi})$ for a normal hydrogen electrode, respectively. From **Figure 2A**, the E_{CBM} and E_{VBM} of $CsPbBr_3$ PQDs were calculated to be −3.4 and −6.0 eV, respectively. The measured band gap of 2.6 eV (from CV data) agreed well with that calculated by PL measurements (2.44 eV). In contrast, $CsPbI_3$ PQDs exhibited a major oxidation peak at ~+0.70 V, as shown in **Figure 2B**. In this case, the E_{CBM} and E_{VBM} were calculated as −3.6 and −5.4 eV, respectively; once again, there was a good coherence between CV and PL values. As expected, we were able to observe not only the major redox peaks occurring at the CBM and VBM, but also additional redox peaks at defect-mediated energy levels.

Supplementary Figures S5A,B show the results of linear sweep voltammetry of $CsPbBr_3$ and $CsPbI_3$ in DCM containing the TBAFP-supporting electrolyte obtained from the GC electrode. The onset oxidation potentials of $CsPbBr_3$ were observed at ~+0.30 and +1.30 V (**Supplementary Figure S5A**). Interestingly, additional oxidation waves were observed similar to those obtained in 3D bulk $CsPbBr_3$ films, as shown in **Supplementary Figure S6**. Such similar oxidation-onset potentials in $CsPbBr_3$ PQDs and 3D bulk $CsPbBr_3$ films indicate identical internal energy levels in the bandgap structure. We speculate that the two internal energy levels oriented from defect-mediated trap sites are interstitial bromide-trapping holes. Previously, it was suggested that the two onset potentials for oxidation correspond to interstitial bromide [(0/+) and (−/0)] transitions (Samu et al., 2019). In the case of $CsPbI_3$, an intense peak was observed at +0.50 V corresponding to the onset potential of oxidation. According to literature, this corresponds to interstitial iodide hole trapping with the (−/0) transition (Samu et al., 2019).

Figure 3 shows the CVs obtained during five consecutive cycles in the range of 0 to +1.8 V and these illustrate the characteristic behavior of colloidal PQD solutions. In the first scan of the PQDs (black line in **Figures 3A,B**), an irreversible anodic wave appeared at +1.5 V for $CsPbBr_3$ and +0.60 V for $CsPbI_3$, but it dramatically diminished in the subsequent scans. These nonrepeatable signals demonstrate irreversible transformation. Similar irreversible transformation could be inferred from CV scans recorded in the range of 0.0 to −1.6 V, as shown in **Supplementary Figure S7**. Therefore, the applied electrochemical bias induces irreversible transformation in both types of PQDs, during which process, they lose their own redox properties.

In Situ Spectroelectrochemical Measurements to Observe Perovskite Quantum Dot Transformation

Encouraged by the irreversible transformation of the PQDs under electrochemical conditions, we analyzed their transformation by *in situ* UV-Vis absorption measurements at different applied potentials. **Figures 4A,B** show examples of the spectroelectrochemical responses of the PQDs at different oxidizing potentials. The absorption band edges of $CsPbBr_3$ (at 497 nm) and $CsPbI_3$ PQDs (at 675 nm) reduced gradually in the range of 0.0 to +1.4 V in 0.2 V increments (**Figures 4C,D**). Absorbance at shorter wavelengths also decreased in the range of 0.0 to +0.6 V. In contrast, the absorbance increased at potentials higher than +0.8 V, as shown in **Figure 4D**. In the case of $CsPbBr_3$ PQDs, absorbance increased at 258 and 272 nm at potentials higher than +0.8 V (green highlights in **Figures**

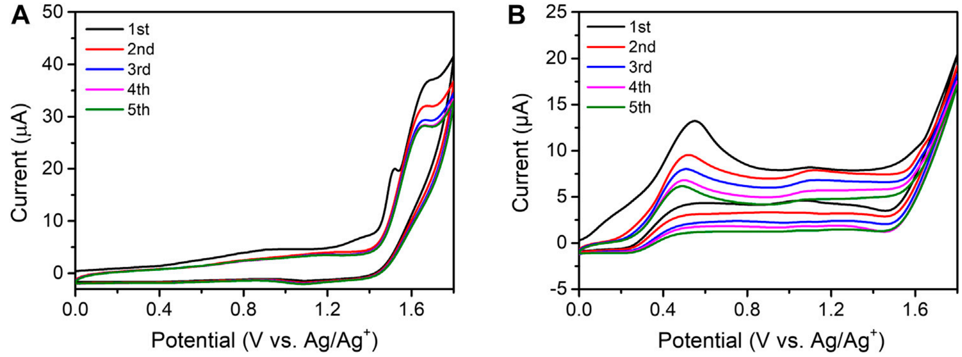

FIGURE 3 | (A) CV of $CsPbBr_3$ in DCM containing 0.1 M TBAFP at 50 mV/s at the GC electrode over five successive cycles. **(B)** CV of $CsPbI_3$ in DCM containing 0.02 M TBAFP at 50 mV/s at the GC electrode over five successive cycles.

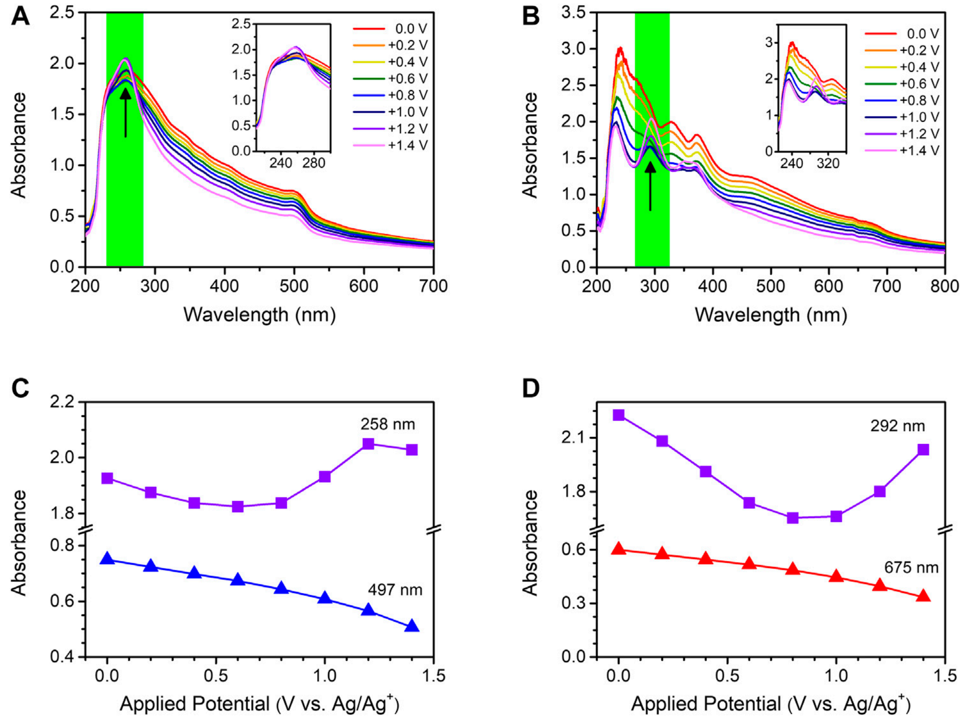

FIGURE 4 | Spectroelectrochemical analysis of **(A)** $CsPbBr_3$ and **(B)** $CsPbI_3$ with respect to the applied potential. The potential was increased from 0.0 to +1.4 V in +0.2 V steps. The insets show magnified views of the UV-Vis absorption spectra, which are highlighted in green. Kinetic trace of the absorption spectra of **(C)** $CsPbBr_3$ and **(D)** $CsPBI_3$. The recorded spectroscopic traces correspond to the data of $CsPbBr_3$ and $CsPBI_3$ in **(A)** and **(B)**, respectively.

4A,C). Meanwhile, the absorbance of $CsPbI_3$ PQDs at 292 and 370 nm decreased in the range of 0.0 to +0.6 V but started to increase at potentials higher than +0.8 V (green highlights in **Figures 4B,D**). This difference in the absorption response of the two PQDs between the band edge and shorter wavelengths is attributed to their transformation to other species. As illustrated in **Figures 2** and **Supplementary Figure S5**, the two PQDs exhibit interstitial halide hole trapping with (−/0) transition due to electrochemical oxidation (Samu et al., 2019). To determine their absorption behavior at shorter wavelengths, it is necessary to assign the corresponding species. Kamat and coworkers demonstrated that the lead-halide complexation chemistry dictates the nature of binding between Pb^{2+} and Br^- and Pb^{2+} and I^- as well as the absorption features of PbX_2, PbX_3^-, and PbX_4^{2-} as multihalide plumbate complexes (Stamplecoskie et al., 2015; Yoon et al., 2016b). In **Supplementary Figure S8A**, absorption of $PbBr_2$ solution and $PbBr_2$ with saturated CsBr solution was shown. The absorption feature of $PbBr_2$ with

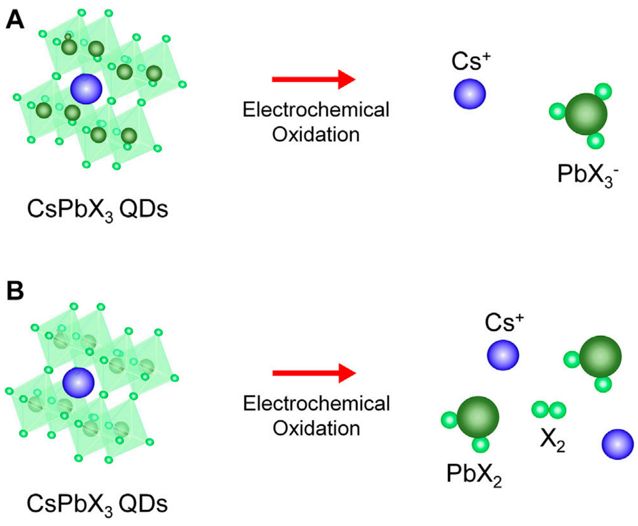

FIGURE 5 | (A,B) Schematic illustrating the proposed reaction mechanism for the irreversible transformation for $CsPbBr_3$ and $CsPbI_3$ PQDs.

saturated CsBr solution indicates absorption of the $PbBr_3^-$ plumbate complex. It can be observed that the initial absorbance at 280 nm due to the absorption of $PbBr_2$ decreased upon the addition of CsBr as a source of bromide. CsBr, when added to $PbBr_2$, resulted in alternative absorption at 258 nm, which can be attributed to the $PbBr_3^-$ species (Yoon et al., 2016b). A new absorption peak at ~258 nm started to appear at voltages higher than +0.8 V, as shown in **Figure 4A**, which indicates that the PQDs transformed into $PbBr_3^-$ (**Supplementary Figure S8A**). The changes occurring in the absorption behavior of $CsPbI_3$ PQDs were similar to those observed for $CsPbBr_3$ PQDs. In $CsPbI_3$ PQDs, two additional absorption peaks at 292 and 370 nm intensified at voltages higher than +0.8 V as compared to continuous decrement at band-edge absorption, as shown in **Figure 4B**. The two absorption peaks from PbI_2 matched the two peaks at 292 and 370 nm (**Supplementary Figure S8B**). The transformation of $CsPbI_3$ PQDs was clearly observed in more defective PQDs with a quantum yield of 10%, as shown in **Supplementary Figure S10**. In contrast, when potentials in the range of 0.0 to −1.2 V were applied to $CsPbBr_3$ and $CsPbI_3$ PQDs at a step size of −0.2 V, the overall absorbance decreased gradually (**Supplementary Figure S9**). These results indicate that, under oxidizing conditions, $CsPbBr_3$ and $CsPbI_3$ PQDs undergo irreversible transformation to $PbBr_3^-$ and PbI_2, respectively.

Irreversible Transformation of Perovskite Quantum Dots to Plumbate Complexes

In situ spectroelectrochemical measurements indicated that halide-mediated hole-trap filling initiated PQD transformation into a plumbate complex. Considering the aforementioned results and literature (Samu et al., 2018; Samu et al., 2019), we propose the following reaction mechanisms to explain such irreversible transformation (**Figure 5**):

$$CsPbX_3 \rightarrow Cs^+ + PbX_{3^-} \tag{2}$$

$$CsPbX_3 + h^+ \rightarrow PbX_2 + Cs^+ + 0.5X_2. \tag{3}$$

Equation 2 describes the separation of the plumbate complex from crystalline $CsPbX_3$ PQDs at an oxidative potential. We hypothesize that separation occurs at small positive voltages by electrostatic reactions, but when the applied voltage increases toward more positive values, which leads to hole-trap filling by interstitial halides, **Eq. 3** becomes dominant. The interstitial halide traps hole and the hole trapping initiates separation of the PQDs, and the PbX_2 can occur. We speculate the trapped hole could induce lattice strain by formation of polaron (Park et al., 2018) and to release the lattice strain, the deformation of perovskite at the strained region so through the *in situ* spectroelectrochemical measurements, formation of PbX_2 could be monitored.

CONCLUSION

In summary, we investigated the photophysical properties of $CsPbX_3$ (X = Br or I) PQDs subjected to an electrochemical potential. The hot-injection process used to synthesize PQDs resulted in an accurate energy-level distribution. Herein, two possible charge-recombination pathways are proposed for these PQDs, i.e., 1) radiative recombination and 2) trap-assisted nonradiative recombination. We studied the redox properties of the PQDs in terms of the CBM, VBM, and interstitial halide-mediated hole trapping via electrochemical measurements. Importantly, the similar energy levels observed in $CsPbBr_3$ PQDs and $CsPbBr_3$ 3D bulk films might be attributed to minor oxidation. This means that the energy-level distribution of the interstitial halide-mediated defects might be similar in the PQDs and bulk film. Furthermore, when an oxidative potential was applied, the PQDs experienced irreversible transformation into PbX_2 or PbX_3^- plumbate complexes, which could be monitored by *in situ* spectroelectrochemical analysis. Such irreversible transformation of the PQDs provides insight into their working mechanism in optoelectronic devices at an applied bias and helps in developing strategies to improve device performance.

DATA AVAILABILITY STATEMENT

The original contributions presented in the study are included in the article/**Supplementary Material**, further inquiries can be directed to the corresponding authors.

AUTHOR CONTRIBUTIONS

DH and SY designed the experiments. CL, KK, and YS performed the experiments. All authors contributed to analysis of the results, data analysis, and preparation of the final manuscript.

FUNDING

This work was supported by the Catholic University of Korea, Research Fund, 2020. DH and KK were supported by the National Research Foundation of Korea (NRF) grant funded by the Korea government (MSIT) 2020R1C1C1006409. CL and SY acknowledge support from the National Research Foundation of Korea (NRF) grant funded by the Korea government (MSIT) 2019R1F1A1062395. SY thank to Prof. Sung-Hwan Han and Prof. Choon Sup Ra for supporting experimental setup to perform synthesis and study photophysical properties of PQDs. The authors thank Jong-in Park and Daegu Science High School for FE-SEM measurements (Hitach SU8010).

SUPPLEMENTARY MATERIAL

The Supplementary Material for this article can be found online at: https://www.frontiersin.org/articles/10.3389/fenrg.2020.605976/full#supplementary-material.

REFERENCES

Agresti, A., Pescetelli, S., Palma, A. L., Martín-García, B., Najafi, L., Bellani, S., et al. (2019). Two-dimensional material interface engineering for efficient perovskite large-area modules. *ACS Energy Lett.* 4, 1862–1871. doi:10.1021/acsenergylett.9b01151

Bishop, J. E., Routledge, T. J., and Lidzey, D. G. (2018). Advances in spray-cast perovskite solar cells. *J. Phys. Chem. Lett.* 9, 1977–1984. doi:10.1021/acs.jpclett.8b00311

Brennan, M. C., Ruth, A., Kamat, P. V., and Kuno, M. (2020). Photoinduced anion segregation in mixed halide perovskites. *Trends Chem.* 2, 282–301. doi:10.1016/j.trechm.2020.01.010

Cardenas-Morcoso, D., Gualdrón-Reyes, A. F., Vitoreti, F., García-Tecedor, M., Yoon, S. J., and Solis de la Fuente, M., (2019). Photocatalytic and photoelectrochemical degradation of organic compounds with all-inorganic metal halide perovskite quantum dots. *J. Phys. Chem. Lett.* 10, 630–636. doi:10.1021/acs.jpclett.8b03849

Chen, H. W., Sakai, N., Ikegami, M., and Miyasaka, T. (2015a). Emergence of hysteresis and transient ferroelectric response in organo-lead halide perovskite solar cells. *J. Phys. Chem. Lett.* 6, 164–169. doi:10.1021/jz502429u

Chen, W., Wu, Y., Yue, Y., Liu, J., Zhang, W., Yang, X., et al. (2015b). Efficient and stable large-area perovskite solar cells with inorganic charge extraction layers. *Science* 350, 944–948. doi:10.1126/science.aad1015

Chen, Y. S., Manser, J. S., and Kamat, P. V. (2015c). All solution-processed lead halide perovskite-BiVO4 tandem assembly for photolytic solar fuels production. *J. Am. Chem. Soc.* 137, 974–981. doi:10.1021/ja511739y

Chen, K., Schünemann, S., Song, S., and Tüysüz, H. (2018). Structural effects on optoelectronic properties of halide perovskites. *Chem. Soc. Rev.* 47, 7045–7077. doi:10.1039/C8CS00212F

Dong, Q., Fang, Y., Shao, Y., Mulligan, P., Qiu, J., Cao, L., et al. (2015). Electron-hole diffusion lengths > 175 μm in solution-grown CH3NH3PbI3 single crystals. *Science* 347, 967–970. doi:10.1126/science.aaa5760

Draguta, S., Thakur, S., Morozov, Y. V., Wang, Y., Manser, J. S., Kamat, P. V., et al. (2016). Spatially non-uniform trap state densities in solution-processed hybrid perovskite thin films. *J. Phys. Chem. Lett.* 7, 715–721. doi:10.1021/acs.jpclett.5b02888

Gebhardt, J., and Rappe, A. M. (2019). Mix and match: organic and inorganic ions in the perovskite lattice. *Adv. Mater.* 31, 1802697. doi:10.1002/adma.201802697

Gualdrón-Reyes, A. F., Rodríguez-Pereira, J., Amado-González, E., Rueda-P, J., Ospina, R., Masi, S., et al. (2020). Unravelling the photocatalytic behavior of all-inorganic mixed halide perovskites: the role of surface chemical states. *ACS Appl. Mater. Interfaces* 12, 914–924. doi:10.1021/acsami.9b19374

Gualdrón-Reyes, A. F., Yoon, S. J., Barea, E. M., Agouram, S., Muñoz-Sanjosé, V., and Meléndez, Á. M. (2019). Controlling the phase segregation in mixed halide perovskites through nanocrystal size. *ACS Energy Lett.* 4, 54–62. doi:10.1021/acsenergylett.8b02207

Han, D., Kim, Y.-R., Oh, J.-W., Kim, T. H., Mahajan, R. K., Kim, J. S., et al. (2009). A regenerative electrochemical sensor based on oligonucleotide for the selective determination of mercury (II). *Analyst* 134, 1857–1862. doi:10.1039/B908457F

Hoke, E. T., Slotcavage, D. J., Dohner, E. R., Bowring, A. R., Karunadasa, H. I., and McGehee, M. D. (2015). Reversible photo-induced trap formation in mixed-halide hybrid perovskites for photovoltaics. *Chem. Sci.* 6, 613–617. doi:10.1039/C4SC03141E

Huang, H., Pradhan, B., Hofkens, J., Roeffaers, M. B., and Steele, J. A. (2020). Solar-Driven metal halide perovskite photocatalysis: design, stability, and performance. *ACS Energy Lett.* 5, 1107–1123. doi:10.1021/acsenergylett.0c00058

Jia, Y., Kerner, R. A., Grede, A. J., Brigeman, A. N., Rand, B. P., and Giebink, N. C. (2016). Diode-pumped organo-lead halide perovskite lasing in a metal-clad distributed feedback resonator. *Nano Lett.* 16, 4624–4629. doi:10.1021/acs.nanolett.6b01946

Kagan, C., Mitzi, D., and Dimitrakopoulos, C. D. (1999). Organic-inorganic hybrid materials as semiconducting channels in thin-film field-effect transistors. *Science* 286, 945–947. doi:10.1126/science.286.5441.945

Kang, D. H., and Park, N. G. (2019). On the current-voltage hysteresis in perovskite solar cells: dependence on perovskite composition and methods to remove hysteresis. *Adv. Mater.* 31, 1805214. doi:10.1002/adma.201805214

Kim, I. S., Pellin, M. J., and Martinson, A. B. (2019). Acid-compatible halide perovskite photocathodes utilizing atomic layer deposited TiO_2 for solar-driven hydrogen evolution. *ACS Energy Lett.* 4, 293–298. doi:10.1021/acsenergylett.8b01661

Kojima, A., Teshima, K., Shirai, Y., and Miyasaka, T. (2009). Organometal halide perovskites as visible-light sensitizers for photovoltaic cells. *J. Am. Chem. Soc.* 131, 6050–6051. doi:10.1021/ja809598r

Koziol, J. (1966). Studies ON flavins IN organic solvents-I*. Spectral characteristics OF riboflavin, riboflavin tetrabutyrate and lumichrome. *Photochem. Photobiol.* 5, 41–54. doi:10.1111/j.1751-1097.1966.tb05759.x

Li, F., Zhou, S., Yuan, J., Qin, C., Yang, Y., Shi, J., et al. (2019). Perovskite quantum dot solar cells with 15.6% efficiency and improved stability enabled by an α-CsPbI3/FAPbI3 bilayer structure. *ACS Energy Lett.* 4, 2571–2578. doi:10.1021/acsenergylett.9b01920

Li, X., Xue, H., and Pang, H. (2017). Facile synthesis and shape evolution of well-defined phosphotungstic acid potassium nanocrystals as a highly efficient visible-light-driven photocatalyst. *Nanoscale.* 9, 216–222. doi:10.1039/c6nr07680g

Mitzi, D. B., Chondroudis, K., and Kagan, C. R. (1999). Design, structure, and optical properties of organic-inorganic perovskites containing an oligothiophene chromophore. *Inorg. Chem.* 38, 6246–6256. doi:10.1021/ic991048k

Mitzi, D. B., Feild, C., Schlesinger, Z., and Laibowitz, R. (1995). Transport, optical, and magnetic properties of the conducting halide perovskite CH3NH3SnI3. *J. Solid State Chem.* 114, 159–163. doi:10.1006/jssc.1995.1023

National Renewable Energy Laboratory (2020). *Best research-cell efficiency chart.* Golden, CO, United States: National Renewable Energy Laboratory. Available at: https://www.nrel.gov/pv/cell-efficiency.html.

Noh, J. H., Im, S. H., Heo, J. H., Mandal, T. N., and Seok, S. I. (2013). Chemical management for colorful, efficient, and stable inorganic-organic hybrid nanostructured solar cells. *Nano Lett.* 13, 1764–1769. doi:10.1021/nl400349b

Park, M., Neukirch, A. J., Reyes-Lillo, S. E., Lai, M., Ellis, S. R., Dietze, D., et al. (2018). Excited-state vibrational dynamics toward the polaron in methylammonium lead iodide perovskite. *Nat. Commun.* 9, 1–9. doi:10.1038/s41467-018-04946-7

Protesescu, L., Yakunin, S., Bodnarchuk, M. I., Krieg, F., Caputo, R., and Hendon, C. H. (2015). Nanocrystals of cesium lead halide perovskites ($CsPbX_3$, X = Cl, Br, and I): novel optoelectronic materials showing bright emission with wide color gamut. *Nano Lett.* 15, 3692–3696. doi:10.1021/nl5048779

Rong, Y., Ming, Y., Ji, W., Li, D., Mei, A., and Hu, Y. (2018). Toward industrial-scale production of perovskite solar cells: screen printing, slot-die coating, and emerging techniques. *J. Phys. Chem. Lett.* 9, 2707–2713. doi:10.1021/acs.jpclett.8b00912

Saba, M., Cadelano, M., Marongiu, D., Chen, F., Sarritzu, V., Sestu, N., et al. (2014). Correlated electron–hole plasma in organometal perovskites. *Nat. Commun.* 5, 1–10. doi:10.1038/ncomms6049

Sadhanala, A., Ahmad, S., Zhao, B., Giesbrecht, N., Pearce, P. M., and Deschler, F. (2015). Blue-green color tunable solution processable organolead chloride-bromide mixed halide perovskites for optoelectronic applications. *Nano Lett.* 15, 6095–6101. doi:10.1021/acs.nanolett.5b02369

Samu, G. F., Balog, Á., De Angelis, F., Meggiolaro, D., Kamat, P. V., and Janáky, C. (2019). Electrochemical hole injection selectively expels iodide from mixed halide perovskite films. *J. Am. Chem. Soc.* 141, 10812–10820. doi:10.1021/jacs.9b04568

Samu, G. F., Scheidt, R. A., Kamat, P. V., and Janáky, C. (2018). Electrochemistry and spectroelectrochemistry of lead halide perovskite films: materials science aspects and boundary conditions. *Chem. Mater.* 30, 561–569. doi:10.1021/acs.chemmater.7b04321

Senanayak, S. P., Yang, B., Thomas, T. H., Giesbrecht, N., Huang, W., and Gann, E. (2017). Understanding charge transport in lead iodide perovskite thin-film field-effect transistors. *Sci. Adv.* 3, e1601935. doi:10.1126/sciadv.1601935

Stamplecoskie, K. G., Manser, J. S., and Kamat, P. V. (2015). Dual nature of the excited state in organic–inorganic lead halide perovskites. *Energy Environ. Sci.* 8, 208–215. doi:10.1039/C4EE02988G

Wang, B., Iocozzia, J., Zhang, M., Ye, M., Yan, S., and Jin, H. (2019). The charge carrier dynamics, efficiency and stability of two-dimensional material-based perovskite solar cells. *Chem. Soc. Rev.* 48, 4854–4891. doi:10.1039/C9CS00254E

Weber, S. A., Hermes, I. M., Turren-Cruz, S.-H., Gort, C., Bergmann, V. W., Gilson, L., et al. (2018). How the formation of interfacial charge causes hysteresis in perovskite solar cells. *Energy Environ. Sci.* 11, 2404–2413. doi:10.1039/C8EE01447G

Yoon, S. J., Stamplecoskie, K. G., and Kamat, P. V. (2016b). How lead halide complex chemistry dictates the composition of mixed halide perovskites. *J. Phys. Chem. Lett.* 7, 1368–1373. doi:10.1021/acs.jpclett.6b00433

Yoon, S. J., Draguta, S., Manser, J. S., Sharia, O., Schneider, W. F., Kuno, M., et al. (2016a). Tracking iodide and bromide ion segregation in mixed halide lead perovskites during photoirradiation. *ACS Energy Lett.* 1, 290–296. doi:10.1021/acsenergylett.6b00158

Yuan, Y., and Huang, J. (2016). Ion migration in organometal trihalide perovskite and its impact on photovoltaic efficiency and stability. *Acc. Chem. Res.* 49, 286–293. doi:10.1021/acs.accounts.5b00420

Zhang, Y., Zhang, S., Zheng, M., and Pang, H. (2015). Ultra-small ZnO nanodots@ functionalized graphene sheets from microwave reaction as effective photocatalysts. *Int. J. Electrochem. Sci.* 10, 8706–8713. Available at: https://http://www.electrochemsci.org/papers/vol10/101008706.pdf

Zhao, Y., and Zhu, K. (2016). Organic-inorganic hybrid lead halide perovskites for optoelectronic and electronic applications. *Chem. Soc. Rev.* 45, 655–689. doi:10.1039/C4CS00458B

Zheng, S., Guo, X., Xue, H., Pan, K., Liu, C., and Pang, H. (2019). Facile one-pot generation of metal oxide/hydroxide@metal-organic framework composites: highly efficient bifunctional electrocatalysts for overall water splitting. *Chem. Commun. (Camb.).* 55, 10904–10907. doi:10.1039/c9cc06113d

Zolfaghari, Z., Hassanabadi, E., Pitarch-Tena, D., Yoon, S. J., Shariatinia, Z., van de Lagemaat, J., et al. (2018). Operation mechanism of perovskite quantum dot solar cells probed by impedance spectroscopy. *ACS Energy Lett.* 4, 251–258. doi:10.1021/acsenergylett.8b02157

Conflict of Interest: The authors declare that the research was conducted in the absence of any commercial or financial relationships that could be construed as a potential conflict of interest.